

## Research Article

# Investigation of Structural, Dielectric, Magnetic and Impedance Spectroscopy of MgO/CuFe<sub>2</sub>O<sub>4</sub> Nanocomposites

Kashif Ali, Asif Ilyas\*

Department of Physics, PMAS Arid Agriculture University Rawalpindi, Pakistan  
E-mail: asifilyas@uaar.edu.pk

**Received:** 24 July 2023; **Revised:** 31 December 2023; **Accepted:** 25 March 2024

**Abstract:** This study investigates the properties of  $(MgO)_x/(CuFe_2O_4)_{1-x}$   $x=10-50$  wt.% nanocomposites (NCPs) prepared by physical mixing of both materials. The crystal structure, phase identification and morphology were analyzed by x-ray Diffraction (XRD) and Scanning Electron Microscope (SEM). The investigation revealed the formation of required phases which are in nanometer dimension (22–54 nm) computed by Debye-Sherrer's formula. Both the real and imaginary parts of dielectric constant ( $\epsilon'$  &  $\epsilon''$ ), a.c. conductivity ( $\sigma_{ac}$ ), and impedance were measured in the frequency range of 1kHz to 2MHz by LCR meter. The  $\epsilon'$  and  $\epsilon''$  revealed a decreasing trend with frequency, while MgO weight fractions in NCPs enhance the permittivity values. The real and imaginary parts of impedance ( $Z'$  &  $Z''$ ) demonstrate a decreasing trend with frequency which is ascribed to increase in  $\sigma_{ac}$ . The complex impedance spectroscopy (CIS) analysis shows semicircular arcs at higher frequency, which are due to electrical transport properties of conducting grains. The effect of MgO contents on magnetic properties were analyzed by measuring  $M-H$  loops at room temperature through vibrating sample magnetometer (VSM). Both the saturation magnetization ( $M_s$ ) and coercivity ( $H_c$ ) values show a decreasing profile with MgO fractions, which are due to increase in nonmagnetic contents and decrease in surface anisotropy respectively.

**Keywords:** dielectric constant; A.C. conductivity; impedance spectroscopy; coercivity and surface anisotropy

## 1. Introduction

The spinel ferrites have been considered as a promising material owing to their inherent dielectric and magnetic properties [1–5]. These inherent outstanding properties made it a suitable candidate for recent scientists and engineers to explore its novel applications by tailoring its properties. Recently, spinel ferrites are being used in different areas of medicines, defense and industry [6–15]. The chemical composition of spinel ferrite is  $M^{2+}Fe_2^{3+}O_4$ , where  $M$  and  $Fe$  are divalent and trivalent cations occupy at tetrahedral ( $A$ ) and octahedral ( $B$ ) sites respectively. This divalent and trivalent metal ions at  $A$  and  $B$  sites made it conductive, where electrons can easily jump under the application of an oscillating electric field. Due to hopping of charge carriers, the conduction process takes place, which can be controlled by shape, grain size and tuning the material properties. This conduction between grain and grain boundaries plays a vital role in defining the materials properties for required applications. Moreover, synthesis methodology, calcinations temperature and time, size and morphology of particles also plays an essential role to tune the magneto-dielectric properties.

Among different types of spinel ferrites,  $CuFe_2O_4$  ( $COF$ ) is the most useful ferrimagnetic material, which crystallizes in two phases: (a) tetragonal and (b) cubic depending upon the distribution of cations among  $A$  and  $B$  sites and calcinations temperature. Tetragonal phase of  $COF$  has the inverse spinel structure, while in cubic phase, some of the  $Cu^{2+}$  ions migrate from  $B$  to  $A$  sites, forcing equal amount of  $Fe^{3+}$  ions to  $B$  sites that gives a mixture

Copyright ©2024 Kashif Ali, et al.

DOI: <https://doi.org/10.37256/3120243425>

This is an open-access article distributed under a CC BY license

(Creative Commons Attribution 4.0 International License)

<https://creativecommons.org/licenses/by/4.0/>

of normal and inverse spinel structures. Moreover, the structure of *COF* is highly distorted because of a cooperative Jahn-Teller effect arising from the electric field produced by nearest neighboring ions known as crystal field [16–18].

The ordinary magnetic and dielectric properties of *COF*; like moderate value of saturation magnetization ( $M_s$ ), low coercive force ( $H_c$ ), minimum value of crystalline anisotropy ( $H_k$ ), moderate values of dielectric constant ( $\epsilon'$ ), impedance ( $Z$ ) and a.c. conductivity ( $\sigma_{a.c}$ ) made it a promising material for recent research [19].

Moreover, due to limiting response in electric and magnetic field, the pristine *COF* cannot be used for essential applications. Therefore, to use the *COF* for required applications, their properties need to be tuned by different techniques like; (a) using dopant of different elements, (b) making its *NCPs* with different metal oxides (*MOs*), hard and soft ferrites, conducting and insulating polymers, graphite and graphene nano-sheets single and multi-walled carbon nano-tubes (*MWCNT*) etc. The selection of host materials for synthesis of *NCPs* depends upon easy and economical availability of raw materials, and small difference in densities to obtain the uniform distribution in the final product. In these materials, metal oxides (*MOs*) are mostly used due to economical availability of raw materials and low time consuming synthesis techniques. Among different types of *MOs*, *MgO* is a promising semiconductor with tuned energy band-gap and broadly involved in expansion of different materials for essential application like high- $T_c$  superconductor material, used in a wide range of microwave (*MW*) and infrared (*IR*) components and in energy storage devices (*ESDs*) [20, 21].

In this research work, the response of *MgO/COF*;  $x = 10\text{--}50$  wt. % *NCPs* in the presence of a magnetic field and an oscillating electric field was studied systematically and observed an improvement in dielectric parameters with enhancement of *MgO* wt. fractions. This improvement in dielectric parameters is ascribed to increase in space charge polarization at the interface of two materials having different values of conductivities. This augmentation in dielectric parameters makes this material to be used in *ESDs* and as a *MW* absorber for electromagnetic (*EM*) shielding applications, where high dielectric loss material is required.

## 2. Experimental and characterization

The nanocomposites of  $(\text{CuFe}_2\text{O}_4)_x/(\text{MgO})_{1-x}$  were synthesized by two step powder mixing method separately synthesized by facile co-precipitation method. The Precursors used with analytical grade are:  $\text{CuCl}_2 \cdot 2\text{H}_2\text{O}$ ,  $\text{FeCl}_3 \cdot 6\text{H}_2\text{O}$ ,  $\text{MgSO}_4 \cdot 7\text{H}_2\text{O}$ , and  $\text{NaOH}$ . In first step, 0.2M ( $\text{CuCl}_2 \cdot 2\text{H}_2\text{O}$ ), 0.4M ( $\text{FeCl}_3 \cdot 6\text{H}_2\text{O}$ ) mixed in 100 ml of distilled water with continuous stirring. 3M solution of  $\text{NaOH}$  added drop wise to adjust  $\text{PH}$ -10~11. The black brown precipitate begin to form, which brought to reaction temperature at 80 °C for one hour with continuous stirring. The precipitate was cooled down to room temperature and washed with distilled water and ethanol to remove the impurities in final sample. The sample still contained water contents which were removed by drying the sample in oven at 100 °C. Finally the dry and dark brown block of sample was obtained, which is grinded in to fine powder. In second step 0.2M ( $\text{MgSO}_4 \cdot 7\text{H}_2\text{O}$ ) dissolve in 100 ml of distilled water and 2M solution of  $\text{NaOH}$  is added dropwise to adjust  $\text{PH}$ -10~11. The obtained precipitates was heated at 60 °C for one hour and washed twice with ethanol. The obtained precipitates were dried and grinded by following the former procedure. The weight percent of *MgO* contents added in *COF* from 10–50% and calcined at 600 °C for five hours to obtain the required nanocomposites.

The crystal structure and morphology of the prepared *COF*, *MgO* and  $(\text{CuFe}_2\text{O}_4)_x/(\text{MgO})_{1-x}$  nanocomposites were analyzed using the x-ray Diffraction (with Cu  $K_\alpha$  radiation of wavelength  $\lambda=1.5405\text{\AA}$  and  $2\theta$  ranging from 20° to 80°, Model JDX-11, of Joel Company Ltd., Japan, operated at 40kV and 30mA) and field Emission Scanning electron Microscope (Tescan,-Vega 03) respectively. The dielectric, electrical and impedance measurement were performed by LCR (IET 7600 Plus Precision) meter Bridge in the frequency range 1 kHz to 2MHz. For the preparation of dielectric measurement, prepared powder was mixed with exact weight percent and pressed with a pressure of 20MPa for five minute to fabricate a pellet of 12mm diameter with 1mm thickness. To confirm the better conducting contact, the pellet was painted with silver paste prior to measurement. The A.C. conductivity was also calculated from measured values of dielectric parameters.

## 3. Results and discussions

### 3.1 Structural and morphological analysis

The crystal structure, purity level and phase identification of  $(\text{MgO})_x/(\text{CF})_{1-x}$  were analyzed by *XRD*. Figure-1 shows the *XRD* pattern of prepared *NCPs* already reported in our previous work [22] and peaks marked with

arrow head, revealed the presence of *MgO* phases. It can also be observed from Fig.1, that the diffraction peaks of *MgO* phase in *NCPs* become more intense with increase in its weight fractions. This rise in intensity is attributed to the presence of large diffracting planes and growth of crystalline phase. Moreover, there is slight shift in peak positions ( $2\theta$  values) was also observed, which is ascribed to the difference in ionic radii and crystal structure that makes stress and strain at the interface of both phases. The average crystallite size was computed by using Debye-Sherrer's formula from diffraction peaks and found to be in the range of 18 to 45 nm [23].

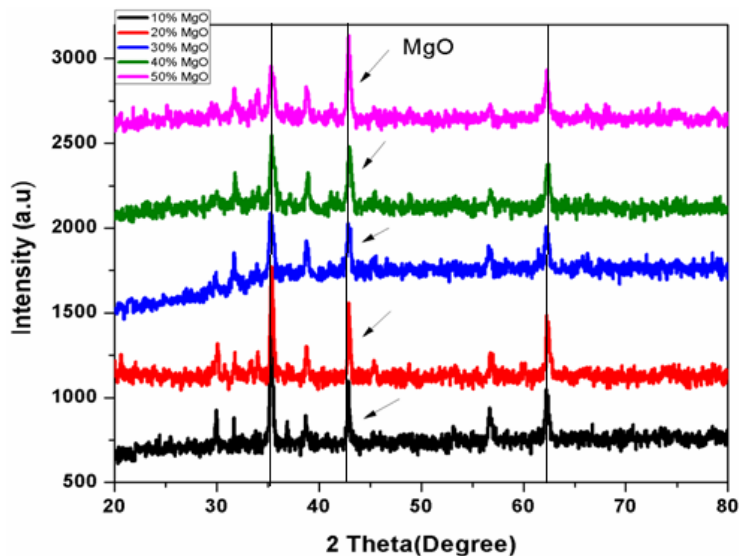


Figure 1. XRD pattern of  $(\text{MgO})_x/(\text{CuFe}_2\text{O}_4)_{1-x}$  ( $x=10\text{-}50$  wt.%) nanocomposites

$$D = \frac{0.9\lambda}{\beta \cos\theta} \quad (1)$$

where  $\lambda$  is the wavelength of x-ray and  $\beta$  is full width at half maximum of the peaks at diffracting angle  $\theta$ .

The *SEM* images in Fig.2 (a &b) shows the morphology of prepared *NCPs* in which both the *CF* magnetic nanoparticles (*MNPs*) and *MgO* show spherical morphology and having size in the range of 29-54nm. Figure-3 (c & d) revealed that, with increase of *MgO* contents from 20-30 wt.% change the morphology of *MgO* (*NPs*) from spherical to nano-spindle which is attributed to change in shape anisotropy in the *NCPs*, that produce the anisotropic unidirectional growth in *MgO* grains. Further increase in *MgO* fractions (40-50 wt.%) enhance the clustering of *MgO* phase and produce an agglomeration of *NPs* as shown and marked in Fig.2 (e & f). Due to the light weight of *MgO* as compared to *COF*, the *MgO* occupies a large space and behaves as a continuous matrix in which *COF* (*MNPs*) are embedded and reduce the magnetic connectivity/continuity of *COF* grains and also demonstrate the coexistence of both phases and are in accordance to the reported *XRD* results.

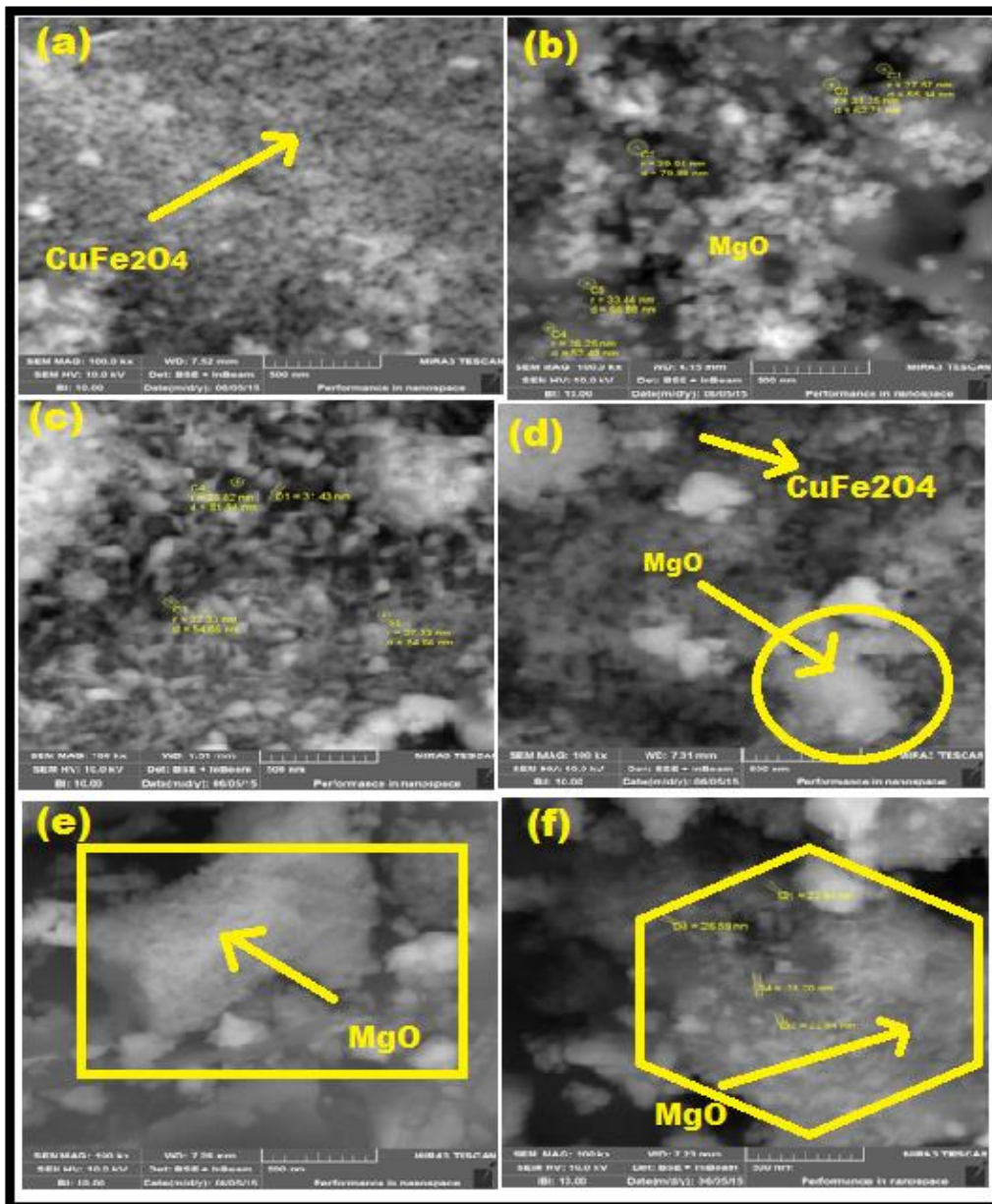


Figure 2. SEM images of  $(MgO)_x/(CuFe_2O_4)_{1-x}$  ( $x=10-50$  wt.%) nanocomposites

### 3.2 Dielectric properties

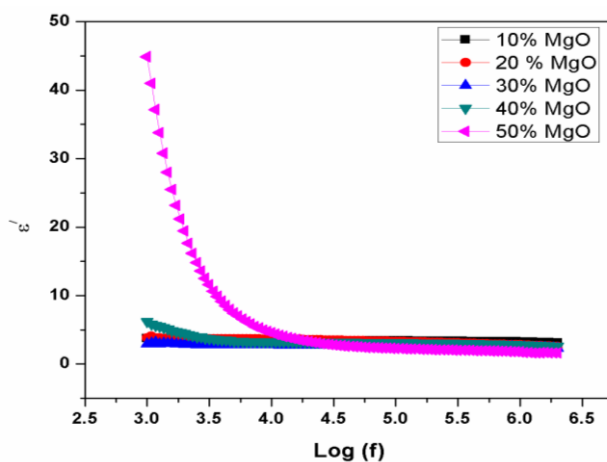
The response of material under an applied oscillating electric field depends on many factors like; grain size, topology, crystal structure and site occupancy of dopant cations between *A* and *B* sites [4, 14, 19]. The Fe oxides based ceramic (like ferrite) material interacts with electric field due to the presence of intrinsic dipole moment and formation of extrinsic dipole established by the hopping of charge carriers. The dielectric profile of ferrites with frequency provide an important information about the behavior of localized electric charge carriers and better understanding of the mechanism of dielectric polarization in ferrites [2, 4, 24].

The  $\epsilon'$  of dielectric constant of  $(MgO)_x/(COF)_{1-x}$  ( $x= 10-50$  wt.%) were measured between frequency range 1kHz to 2MHz as shown in Fig-3(a). It can be observed that  $\epsilon'$  go through a sharp decrease with frequency up to  $\log(4)$  Hz, and then shows a constant behavior at higher frequencies  $\geq \log(4)$  Hz. This higher value of  $\epsilon'$  at lower frequency is attributed to the interfacial polarization because grains are active at low frequency and due to conducting nature of grains; the charges moves and pile up at grain boundaries and enhance the space charge polarization. Therefore a large value of electric energy will be stored in the material at low frequency. At high frequency, the insulating grain boundaries become active and resist the flow of charge carriers due to high value of resistance. Moreover, at higher frequency, the interfacial dipoles cannot respond with varying frequency of

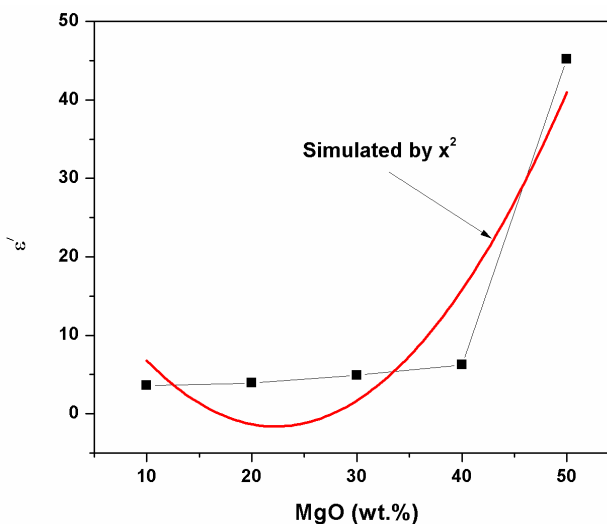
applied field. Because, at higher frequency, the relaxation time of dipoles and A.C. field may not synchronize to each other, therefore a constant behavior of  $\epsilon'$  were observed.

Furthermore, Fig.3 (b) shows a compositional dependence variation in  $\epsilon'$  with  $MgO$  wt. % at 1 kHz. There is a monotonic increasing trend in the values of  $\epsilon'$  (3.6 to 45.22), and follow  $x^2$  law. This enhancement in  $\epsilon'$  is attributed to the presence of secondary phase of  $COF$  in  $NCPs$  that produce the charge accumulation at the interface due to the difference in conductivity ( $\sigma_1, \sigma_2$ ) of both materials. This accumulation of charges produces the interfacial polarization and hence enhances the  $\epsilon'$  accordingly [9, 17].

The behavior of  $\epsilon''$  with frequency is shown in fig.4 (a), all the samples show a decreasing trend with frequency. This behavior of dielectric loss with increasing frequency can be explained on the basis of Koop's model [25]. Moreover, the losses in  $NCPs$  are considered to be caused by domain wall motion. At low values of frequency the domain wall moves and produces heating effect due to the dissipation of energy by friction. At higher frequencies, losses are found to be low because domain wall motion was inhibited [25, 26]. Furthermore, the values of  $\epsilon''$  also decreases, when the polarization lags behind the applied alternating field and may be due to the crystalline defects like grain boundaries, impurities, and imperfections in the crystal lattice [15, 24]. In Fig.4 (a), there is a Peaking/resonance behavior was observed at 50wt. % composition. This resonance behavior can be explained by Rezlescu model [27]. This peaking behavior at log (3.5) kHz appeared, when the hopping frequency between the  $Fe^{2+}$  and  $Fe^{3+}$  ions exactly matches with the frequency of the applied external oscillating field. This condition for resonance in the  $\epsilon''$  in 50 wt. % composition is given by the relation:



a



b

**Figure 3.** (a): Real part of  $(MgO)_x/(CuFe_2O_4)_{1-x}$  nanocomposites from 1kHz-2MHz, (b): Compositional dependence of  $\epsilon'$  with  $MgO$  wt.% ( $x=10-50$  wt.%)

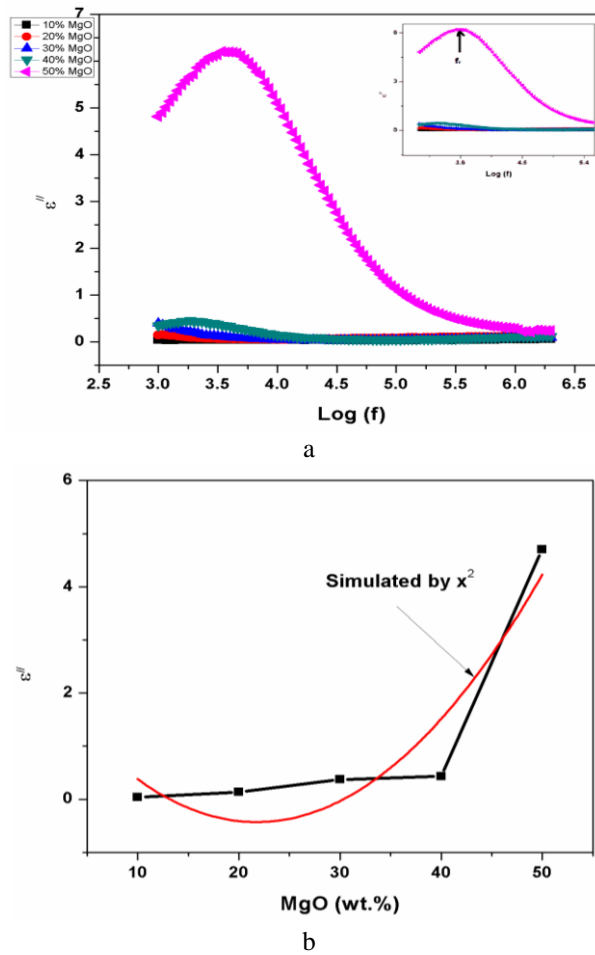


**Figure 4.** (a): Imaginary part of  $(MgO)_x/(CuFe_2O_4)_{1-x}$  nanocomposites from 1kHz-2MHz, (b): Compositional dependence of  $\epsilon''$  with MgO wt. % ( $x=10-50$  wt. %)

$$\omega\tau = 1 \quad (2)$$

where  $\omega=2\pi f_{\max}$  and  $\tau$  is the relaxation time and a relation between the relaxation time to the jumping probability per unit time is given as.

$$\tau = 1/2p \quad (3)$$

or

$$f_{\max} \propto p \quad (4)$$

Consequently, from the above relation it is evident that, resonance peak is observed when the jumping frequency of electrons exchange between  $Fe^{2+}$  and  $Fe^{3+}$  becomes approximately equal to the frequency of applied field. The composition for  $x \leq 40$  wt. % did not show like this behavior due to insufficient availability of  $Fe^{2+}$  ions. At 50 wt. % there is large availability of  $Fe^{2+}$  ions that enhance the probability of jumping of charge carriers between  $Fe^{3+}$  and  $Fe^{2+}$  at octahedral sites.

Fig.4 (b) shows the variations of  $\epsilon''$  with MgO wt. %, at 1 kHz, and it can be observed that the values of  $\epsilon''$  increases with addition of MgO wt. fractions in NCPs. This increase in the values of  $\epsilon''$  is attributed to the enhancement in interfacial charge polarization. The increase in concentration of MgO, enhances the interfaces, which was also observed from SEM images in fig.2 and hence there is more space available for the accumulation of charges. This accumulation of charges is responsible to enlarge  $\epsilon''$  values accordingly. Generally, a material present high storage of energy also allows big losses and vice versa. Hence the variation in the values of  $\epsilon''$  with frequency and composition are consistent with the acquired values of  $\epsilon'$  as shown in fig.3 (a & b).

### 3.3 A.C. conductivity

The kinetic of charge carriers under an applied alternating field is called  $\sigma_{a.c.}$ . The behaviour of  $\sigma_{ac}$  as a function of frequency (1kHz to 2MHz) is shown in fig.5. All the compositions show an increasing trend in  $\sigma_{ac}$  with frequency and follow the power law  $\sigma(\omega) = A \omega^s$  [28–30], where  $A$  is a parameter having units of conductivity

and  $s$  is the slope of the  $\sigma_{ac}$  profile. The  $\sigma_{ac}$  can be determined from dielectric parameters using the following relation [15];

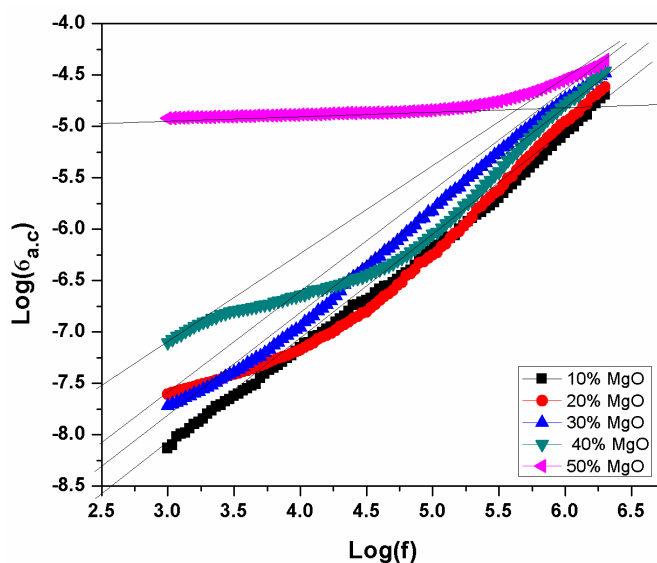


Figure 5. A.C. Conductivity of  $(MgO)_x/(CuFe_2O_4)_{1-x}$  nanocomposites from 1kHz-2MHz

$$\sigma_{ac} = 2\pi\epsilon_0\epsilon'f \tan \delta \quad (5)$$

where “ $f$ ” is the frequency of the applied field,  $\epsilon_0$  is the permittivity of free space,  $\epsilon'$  is the real part of dielectric constant,  $\tan\delta$  is the dissipation factor ( $DF$ ), and  $\sigma_{ac}$  is the conductivity [15, 24]. Figure 5 shows the variation of  $\sigma_{ac}$  with frequency in the range of 1kHz to 2MHz. In the present study,  $\sigma_{ac}$  with frequency shows a linear behavior, demonstrating the small polaron conduction. This linear increase in  $\sigma_{ac}$  with frequency is attributed to the conduction by electron exchange between the ions of same element at different valence states. Furthermore, the frequency dependence of  $\sigma_{ac}$  can also be explained with the help of the Maxwell-Wagner two-layer model. According to this model, grain boundaries are insulating and become active at low frequency and offers high resistance to the charge carriers. On the other hand, due to conducting nature of grains which are active at higher frequency, promotes the electron exchange between  $Fe^{3+}$  and  $Fe^{2+}$  cations at octahedral sites. Hence, this hopping of charge carriers also contribute in the enhancement of  $\sigma_{ac}$  values [15–19].

The variation of  $\sigma_{ac}$  with composition  $(MgO)_x/(COF)_{1-x}$  ( $x = 10$  to 50 wt.%) also shows an increasing trend with  $MgO$  contents. This increasing trend in  $\sigma_{ac}$  is attributed to increase in hopping conduction at octahedral sites and also decreases in band gap due to impurity states of  $MgO$ . These impurity states also promote the band conduction along with hopping conduction and hence, results in increase in conductivity values [15].

## 4. Impedance properties

In the presence of an external sinusoidal signal that perturbs a semiconducting material and the frequency response recorded as impedance  $Z(\omega)$ . The applied potential is given as;

$$V = V_0 e^{i\omega t} \quad (6)$$

The output current of the system is represented as;

$$I = I_0 e^{i(\omega t + \phi)} \quad (7)$$

where  $\omega = 2\pi f$  is angular frequency and according to Ohm’s law, the complex impedance ( $Z^*$ ) of the circuit at any frequency  $f$  is given as:

$$\begin{aligned} Z^* &= \frac{V}{I} = \frac{V_0}{I_0} e^{-i\phi} = Z e^{-i\phi} = Z \cos\phi - iz \sin\phi \\ &= Z' - iZ'' \end{aligned} \quad (8)$$

where  $Z'$  &  $Z''$ , are the real and imaginary parts of the impedance respectively and offer the resistive and reactive participation to the conductivity. Impedance Spectroscopy is an important technique for explaining the electrical properties of materials [33]. Fig. 6 (a & b) shows the variation of  $Z'$  and  $Z''$  with frequency from 1kHz-2MHz. It is revealed from fig.6 that the impedance value is high at low frequency, then decreases sharply and become constant at higher frequency. This decrease in impedance at higher frequency is due to increase in conductivity because more charges are promoted at higher frequency which enhances the conductivity as shown in Fig.5. Complex

impedance plots (*CIP*) is a vital tool that create relationship between microstructures and the electrical properties of polycrystalline ceramic material. Most of the ceramic materials contain grains and grain boundaries regions, which exhibit different electrical properties due to difference in electrical resistance [35, 36]. *CIP* also called as Nyquist diagrams, which gives a complete contribution of microstructure (grains and grains boundary) resistances [37, 38]. Since polycrystalline materials generally show inter granular or grain-boundary impedances; they can be represented by the equivalent circuit shown in Fig.7. The circuit consists of a series array of two sub-circuits; one represents grain effects and the other represents the effect from grain boundaries. Each sub-circuit is composed of a resistor and capacitor connected in parallel. Let  $R_g$ ,  $R_{gb}$ ,  $C_g$  and  $C_{gb}$  are the resistances and capacitances of grains and grain boundaries respectively [37–40]. Figure-8 shows the complex impedance plots (Cole-Cole plots) at room temperature for all compositions. It is indicated from graphs that there is only one semicircular arc at higher frequency which is attributed to the contribution from grains [41–44]. The total impedance ( $Z$ ) of equivalent circuit is given as;

$$Z = \frac{1}{R_g + j\omega C_g} + \frac{1}{R_{gb} + j\omega C_{gb}} = Z' - jZ'' \quad (9)$$

where

$$Z' = \frac{R_g}{1 + (\omega R_g C_g)^2} + \frac{R_{gb}}{1 + (\omega R_g C_g)^2} \quad (10)$$

&

$$Z'' = \frac{\omega R_g^2 C_g}{1 + (\omega R_g C_g)^2} + \frac{\omega R_g^2 C_{gb}}{1 + (\omega R_g C_g)^2} \quad (11)$$

Figure-8 shows that, the grain contribution increases in all the composition;  $x=10$ –50 wt. % due to increase in grain size. This increase in grain size, reduce the area of oxygen rich layer (grain boundaries) and also promotes the hopping of charge carriers at higher frequency [45].

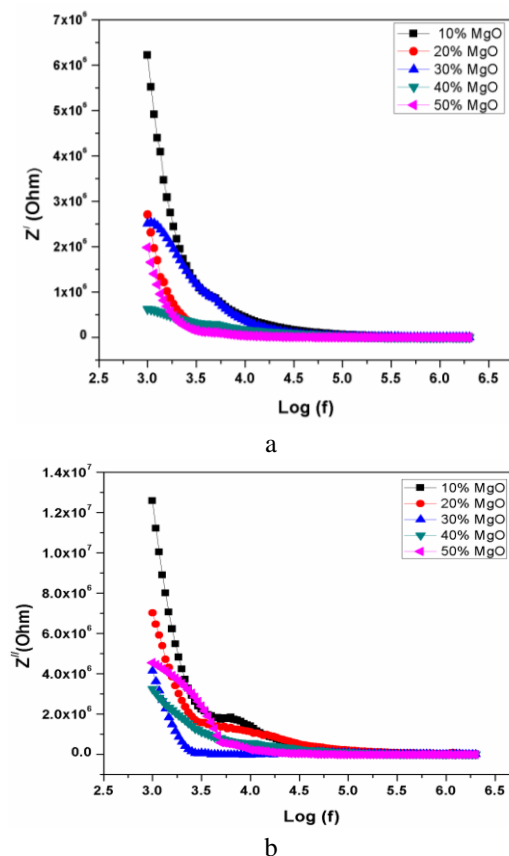


**Figure 6.** (a): Real part of impedance of  $(\text{MgO})_x/(\text{CuFe}_2\text{O}_4)_{1-x}$  nanocomposites, (b): Imaginary part of impedance of  $(\text{MgO})_x/(\text{CuFe}_2\text{O}_4)_{1-x}$  nanocomposites

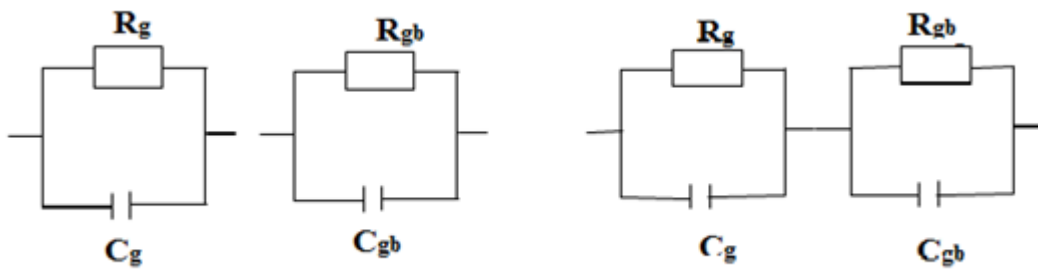


Figure 7. Equivalent circuit diagram describing the grain and grain boundaries resistance

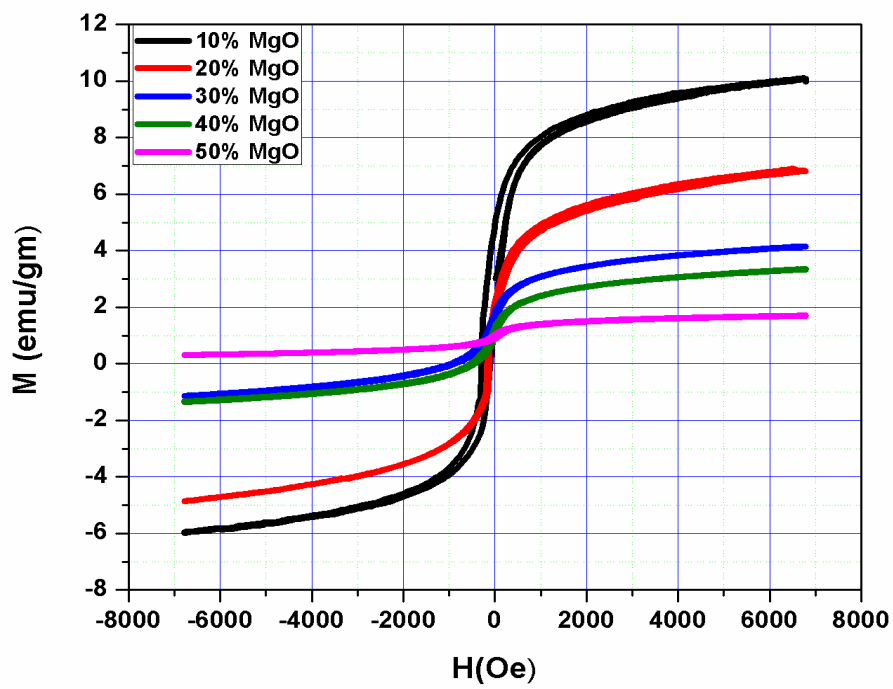


Figure 8. M/H loop of  $(\text{MgO})_x/(\text{CuFe}_2\text{O}_4)_{1-x}$  nanocomposite

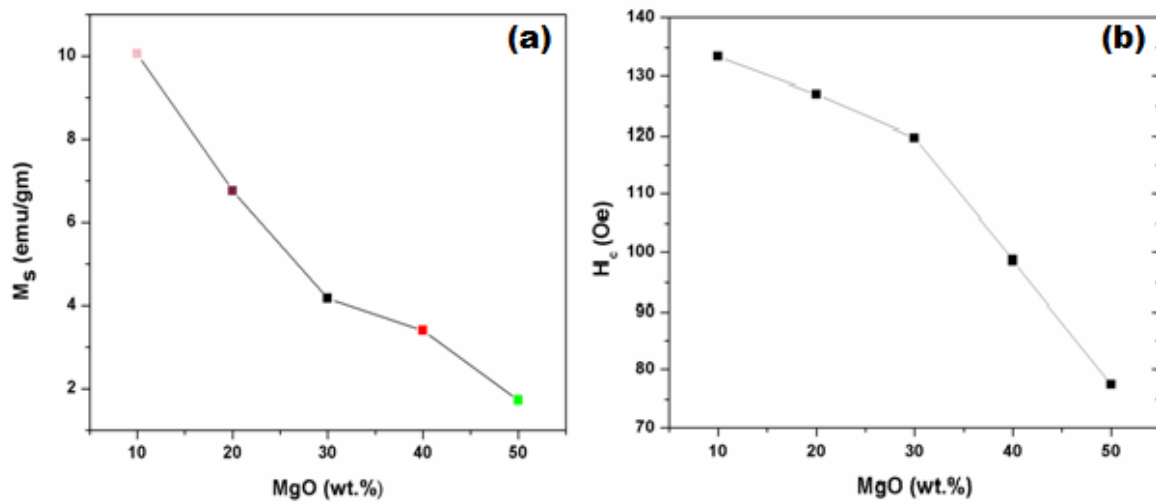


Figure 9. Variation of MgO wt. % on (a) Saturation Magnetization (b) Coercivity

## 5. Magnetic properties

In order to study the response of magnetic field on the prepared *NCPs*, the *M/H* loops were measured under an applied magnetic field of  $\pm 7$  kOe at room temperature. Moreover, the effect of *MgO* contents on the magnetic properties like;  $M_s$  and  $H_c$  were also measured by *M-H* loops. Figure-8 shows that, all the compositions revealed the same magnetic behavior of ferrites and a monotonic decrease in the values of  $M_s$  and  $H_c$  were also observed with *MgO* wt. fractions as shown in fig.8. The magnetic properties of ferrite based materials depend on grain size, types of dopant cations at tetrahedral and octahedral site, wt. fraction of magnetic/nonmagnetic contents and A-B exchange interaction. The decrease in  $M_s$  value with the addition of nonmagnetic contents of *MgO* is shown in table-I. This decrease in  $M_s$  is attributed to the increase in the non-magnetic fractions in the *NCPs*. Secondly, the diamagnetic nature of  $Mg^{2+}$  ions ( $0\mu_B$ ) as compared to weak magnetic nature of  $Cu^{2+}$  ( $1\mu_B$ ) ions is responsible factor for this decrease in  $M_s$  as shown in fig. 9(a). Moreover, the same behavior with  $H_c$  values was also observed in fig.8 which can be explained that, with increase in *MgO* (non-magnetic) wt. fractions, the shape of particles changes from spherical to nanospindle. Moreover, the increase in particle size and clustering of *MgO* phase reduce the surface anisotropy of the whole system. This decrease in surface anisotropy requires a low value of field to magnetize/demagnetize the magnetic domains and hence reduce the coercivity of the entire material [46–48]. Thus the larger grain size and reduction in surface anisotropy play a key role to diminish the coercivity of *NCPs* as shown in fig. 9 (b).

## 6. Conclusion

The  $(MgO)_x/(COF)_{1-x}$ ;  $x=10-50$ wt.% were successfully synthesized by mixing of both materials. The structural, electrical transport, dielectric, magnetic and impedance properties were studied in detailed. The  $\epsilon'$  shows the normal dispersion of ferrite material. The  $\epsilon'$  and  $\sigma_{ac}$  increases with *MgO* weight fractions which is attributed to the accumulation of charges at the interface of two different permittivity zones. The  $\epsilon''$  also shows increasing behavior due to the loss of energy released during domain walls motion and orientation of interfacial polarization. The real and imaginary parts ( $Z'$  and  $Z''$ ) of impedance shows decreasing trend with frequency and *MgO* weight fractions which is ascribed to increase in the values of  $\sigma_{ac}$ . The semicircular arc at higher frequency in complex impedance plot confirms the conduction of charge carriers from grains. The *M-H* loops show normal behavior of ferrimagnetic with decreasing values of  $M_s$  and  $H_c$ . This higher values of  $\epsilon'$  and  $\epsilon''$  make this *NCPs*, a suitable material in the fabrication of *MW* absorption coatings for EM shielding applications.

## References

- [1] Džunuzović, A.S.; Ilić, N.I.; Vijatović Petrović, M.M.V.; Bobić, J.D.; Stojadinović, B.; Dohčević-Mitrović, Z.; Stojanović, B.D. Structure and properties of Ni–Zn ferrite obtained by auto-combustion method. *J. Magn. Magn. Mater.* 2018, 374, 245–251.
- [2] F. Motahari, M.R. Mozdianfard, F. Soofivand, M.S. Niasari, NiO nanostructures: synthesis, characterization and photocatalyst application in dye pollution wastewater treatment. *RSC Adv.* 4, 27654 (2014).
- [3] Limaye, M. V.; Singh, S. B.; Date, S. K.; Kothari, D.; Reddy, V. R.; Gupta, A.; Sathe, V.; Choudhary, R.; Kulkarni, S. K. High coercivity of oleic acid capped CoFe<sub>2</sub>O<sub>4</sub> nanoparticles at room temperature. *J. Phys. Chem. B*, 113, 9070–9076 (2009).
- [4] Mazario, E.; Menéndez, N.; Herrasti, P.; Cañete, M.; Connord, V.; Carrey, J. Magnetic hyperthermia properties of electro synthesized cobalt ferrite nanoparticles. *J. Phys. Chem. C*, 117, 11405–11411 (2013).
- [5] Ramana, C.V.; Kolekar, Y.D.; Bharathi, K.K.; Sinha, B.; Ghosh, K. Correlation between structural, magnetic, and dielectric properties of manganese substituted cobalt ferrite. *J. Appl. Phys.* 2013, 114, <https://doi.org/10.1063/1.4827416>.
- [6] Prathapani, S.; Jayaraman, T.V.; Varaprasadarao, E.K.; Das, D. Structural and ambient/sub-ambient temperature magnetic properties of Er-substituted cobalt-ferrites synthesized by sol-gel assisted auto-combustion method. *J. Appl. Phys.* 2014, 116, <https://doi.org/10.1063/1.4889929>.
- [7] K. Ashwini, H. Rajanaika, K.S. Anantharaju, H. Nagab hushanad, P.A. Reddy, K. Shetty, K.R.V. Mahesh, Synthesis and characterization of as-formed and calcined MnFe<sub>2</sub>O<sub>4</sub>
- [8] nanoparticles: a comparative study of their antibacterial activities. *Mater. Today Proc.* 4, 11902-11909 (2017).

- [9] Mukherjee, D.; Hordagoda, M.; Hyde, R.; Bingham, N.; Srikanth, H.; Witanachchi, S.; Mukherjee, P. Nanocolumnar Interfaces and Enhanced Magnetic Coercivity in Preferentially oriented Cobalt Ferrite Thin Films Grown Using Oblique-Angle Pulsed Laser Deposition. *ACS Appl. Mater. Interfaces* **2013**, *5*, 7450–7457, <https://doi.org/10.1021/am401771z>.
- [10] *Appl. Mater. Interfaces*, *5*, 7450–7457 (2013).
- [11] Kamala Bharathi, K.; Markandeyulu, G.; Ramana, C. V. Structural, magnetic, electrical, and magnetoelectric properties of Sm- and Ho-substituted nickel ferrites. *J. Phys. Chem. C*, *115*, [12] 554–560 (2011).
- [13] Mikalauskaitė, A.; Kondrotas, R.; Niaura, G.; Jagminas, A. Gold-Coated Cobalt Ferrite Nanoparticles via Methionine-Induced Reduction. *J. Phys. Chem. C* **2015**, *119*, 17398–17407, <https://doi.org/10.1021/acs.jpcc.5b03528>.
- [14] Monaji, V. R.; Das, D. Influence of Zr doping on the structural, magnetic and magnetoelastic properties of cobalt- ferrites. *J. Alloys Compd.*, *634*, 99–103 (2015).
- [15] Shaikh, P. A.; Kambale, R. C.; Rao, A. V.; Kolekar, Y. D. Structural, magnetic and electrical properties of Co–Ni–Mn ferrites synthesized by co-precipitation method. *J. Alloys Compd.*, *492*, 590–596 (2010).
- [16] Kahn, M.L.; Zhang, Z.J. Synthesis and magnetic properties of CoFe<sub>2</sub>O<sub>4</sub> spinel ferrite nanoparticles doped with lanthanide ions. *Appl. Phys. Lett.* **2001**, *78*, 3651–3653, <https://doi.org/10.1063/1.1377621>.
- [17] Pandit, R.; Sharma, K. K.; Kaur, P.; Kumar, R. Cation distribution controlled dielectric, electrical and magnetic behavior of Ln<sup>3+</sup> substituted cobalt ferrites synthesized via solid-state reaction technique. *Mater.Chem. Phys.*, *148*, 988–999 (2014).
- [18] Ge, Y.-C.; Wang, Z.-L.; Yi, M.-Z.; Ran, L.-P. Fabrication and magnetic transformation from paramagnetic to ferrimagnetic of ZnFe<sub>2</sub>O<sub>4</sub> hollow spheres. *Trans. Nonferrous Met. Soc. China* **2019**, *29*, 1503–1509, [https://doi.org/10.1016/s1003-6326\(19\)65057-0](https://doi.org/10.1016/s1003-6326(19)65057-0).
- [19] Chand, P.; Vaish, S.; Kumar, P. Structural, optical and dielectric properties of transition metal (MFe<sub>2</sub>O<sub>4</sub>; M = Co, Ni and Zn) nanoferrites. *Phys. B Condens Matter*. 2017, *524*, 53–63.
- [20] Jeevanandam, J.; Barhoum, A.; Chan, Y.S.; Dufresne, A.; Danquah, M.K. Review on nanoparticles and nanostructured materials: History, sources, toxicity and regulations. *Beilstein. J. Nanotechnol.* 2018, *9*, 1050–1074.
- [21] Asghar, K.; Qasim, M.; Das, D. Preparation and characterization of mesoporous magnetic MnFe<sub>2</sub>O<sub>4</sub>@mSiO<sub>2</sub> nanocomposite for drug delivery application. *Mater. Today Proc.* 2020, *26*, 87–93.
- [22] Sivakumar, P.; Ramesh, R.; Ramanand, A.; Ponnusamy, S.; Muthamizhchelvan, C. Synthesis and characterization of NiFe<sub>2</sub>O<sub>4</sub> nanoparticles and nanorods. *J. Alloy Comp.* 2013, *563*, 6–11.
- [23] X. Gerbaux, A. Hadni, M. Tazawa, J.C. Villegier, Far-infrared spectra of magnesium [24] oxide, *J. C. Appl. Opt.* 33 57-59(1994).
- [25] T.J. Edwards, D. Walsh, M.B. Spurr, C.F. Rae, M.H. Dunn, P.G. Browne, Compact [26] source of continuously and widely-tunable terahertz radiation, *Opt. Express* 14 1582-1589 (2006).
- [27] Iqbal, M.J.; Yaqub, N.; Sepiol, B.; Ismail, B. A study of the influence of crystallite size on the electrical and magnetic properties of CuFe<sub>2</sub>O<sub>4</sub>. *Mat. Res. Bull.* 2011, *46*, 1837–1842.
- [28] X. Zhao, L. Wang, X. Xu, Xi. Lei, S. Xu, F. Zhang, Fabrication and photocatalytic properties of novel ZnO/ZnAl<sub>2</sub>O<sub>4</sub> nanocomposite with ZnAl<sub>2</sub>O<sub>4</sub> dispersed inside ZnO network, *Mater. Interfaces, Electrochem. Phenom.* 12597, (2011).
- [29] Kaur, B.; Singh, L.; Annapu, V.; Reddy, Yong Jeong, D.; Dabra, N.; Jasbir S.; Hundal, AC Impedance Spectroscopy, Conductivity and Optical Studies of Sr doped Bismuth Ferrite Nanocomposites, *Int. J. Electrochem. Sci.*, *11* (2016) 4120 – 4135.
- [30] Koop, C.G.; On the dispersion of resistivity and dielectric constant of some semiconductors at audio frequencies, *Phys. Rev.* *83* ;121. (1951)
- [31] Murthy, V.R.K.; Sobhanadari, J.; Dielectric properties of some nickel-zinc ferrites at Radio frequency, *J. Phys. Status Solidi* *36*) 133–135, (1976).
- [32] N. Rezlescu, E. Rezlescu, Dielectric Properties of Copper Containing Ferrites, *Phys. Status Solidi* (a) *23* (1974) 575-582.
- [33] Status Solidi (a) *23* (1974) 575-582.
- [34] Singh, A.K.; Goel, T.C.; Mendiratta, R.G.; Thakur, O.P.; Prakash, C.; Dielectric properties of Mn-substituted Ni-Zn ferrites, *J. Appl. Phys.* *91* (2002) 6626– 6629.
- [35] Kolekar, Y. D.; Sanchez, L. J.; Ramana, C. V. Dielectric relaxations and alternating current conductivity in manganese substituted cobalt ferrite. *J. Appl. Phys.* 2014, *115*, 144106.
- [36] Koops, C. G. On the dispersion of resistivity and dielectric constant of some semiconductors at audio-frequencies. *Phys. Rev.* 1951, *83*, 121–124.
- [37] Kambale, R. C.; Shaikh, P. A.; Bhosale, C. H.; Rajpure, K. Y.; Kolekar, Y. D. The effect of Mn substitution on the magnetic and dielectric properties of cobalt ferrite synthesized by an autocombustion route. *Smart Mater.Struct.* *18* (2009) (1–7).
- [38] Mansingh, A.; Dhawan, V.K.; AC conductivity of V<sub>2</sub>O<sub>5</sub>-TeO<sub>2</sub> glasses, *J. Phys. C Solid State Phys.* *16* (1983) 1675–1683.

- [39] Ata-Allah, S.S.; Kaiser, M.; Semiconductor-to-metallic transition in Cusubstituted Ni–Mn ferrite J, Phys. Status Solidi 201 (2004) 3157–3165.
- [40] N.F. Mott, E.A. Davis, Electronic Processes in Non-Crystalline Materials, 2nd edn., Taylor & Francis, 1979.
- [41] K.W. Wagner, Dielectric relaxation in distributed dielectric layers, Ann. Phys. 40 (1913) 817–85
- [42] Vinosha, P.A.; Manikandan, A.; Preetha, A.C.; Dinesh, A.; Slimani, Y.; Almessiere, M.A.; Baykal, A.; Xavier, B.; Nirmala, F.G. Review on recent advances of synthesis, magnetic properties, and water treatment applications of cobalt ferrite nanoparticles and nanocomposites. J. Supercond. Nov. Magn. 2021, 34, 995–1018.
- [43] Sindhu, S.; Anantharaman, M.R.; Thampi, B.P.; Malini, K.A.; Kurain, P.; Evaluation of a.c. conductivity of rubber ferrite composites from dielectric measurements, Bull. Mater.Sci. 25 (2002) 599–605.
- [44] Devan, R. S.; Kolekar, Y. D.; Chougule, B. K. Effect of cobalt substitution on the properties of nickel–copper ferrite. J. Phys.: Condens. Matter 2006, 18, 9809–9821.
- [45] Sinclair, D. C.; and West, A. R.; Impedance and modulus spectroscopy of semiconducting BaTiO<sub>3</sub> showing positive temperature coefficient of resistance J. Appl. Phys. 66, 3850 (1989).
- [46] Macdonald, J. R., Impedance Spectroscopy (Wiley, New York, 1987).
- [47] Sinclair, D. C.; Adams, T. B.; Morrison, F. D. and West, A. R., CaCu<sub>3</sub>Ti<sub>4</sub>O<sub>12</sub>:CaCu<sub>3</sub>Ti<sub>4</sub>O<sub>12</sub>: One-step internal barrier layer capacitor Appl. Phys.Lett. 80, 2153 (2002).
- [48] Younas, M.; Nadeem, M.; Atif, M.; Grossinger, R.; Metal-semiconductor transition in
- [49] NiFe<sub>2</sub>O<sub>4</sub> nanoparticles due to reverse cationic distribution by impedance spectroscopy, J. Appl. Phys. 109 (2011) 093704.
- [50] Das, R.; Sarkar, T. and Mandal, K.; J. Phys. D: Appl. Phys., 45 (2012) 455002 .
- [51] Kambale, R. C.; Shaikh, P. A.; Bhosale, C. H.; Rajpure, K. Y.; Kolekar, Y. D. The effect of Mn substitution on the magnetic and dielectric properties of cobalt, synthesized by an autocombustion route. Smart Mater.Struct.2009, 18, 115028 (1-7).
- [52] Bhavikatti, A. M.; Kulkarni, S.; Lagashetty, A. Evaluation of AC conductivity and dielectric behavior of cobalt ferrite. Int. J. Eng. Sci. Technol. 2014, 3, 5985-5991.
- [53] K. Maaz, A. Mumtaz, S. K. Hasanain, A. Ceylan (2007), Synthesis and magnetic properties of cobalt ferrite (CoFe<sub>2</sub>O<sub>4</sub>) nanoparticles prepared by wet chemical route, J. Magn. Magn. Mater, Vol. 308, pp.289-296.(2006).
- [54] L. Zhao, H. Yang, L. Yu, Y. Cui, X. Zhao, S. Feng (Study on magnetic properties of nanocrystalline La-, Nd-, or Gd-substituted Ni–Mn ferrite at low temperatures, J. Magn. Magn. Mater, Vol. 305, pp.91-94. K. Lawrence, K. Manoranjan (2011),
- [55] Influence of Al<sup>3+</sup> ion concentration on the crystal structure and magnetic anisotropy of nanocrystalline spinel cobalt ferrite, J. Magn. Magn. Mater, Vol. 323, pp.2042-2048.